





Mutual stabilization of charge-density-wave and monoclinic distortion in sulfur at high pressuresOwen Moulding ^{1,2,3,*}, Lewis J. Conway,^{4,5} Israel Osmond,¹ Sam Cross,¹ Andreas Hermann ⁴,
Jonathan Buhot ¹ and Sven Friedemann^{1,†}¹*H.H. Wills Laboratory, Tyndall Avenue, University of Bristol, Bristol BS8 1TL, United Kingdom*²*Institut Néel CNRS/UGA UPR2940, MCBT, 25 Rue des Martyrs BP 166, 38042 Grenoble Cedex 9, France*³*Max-Planck Institute for Chemical Physics of Solids, Nöthnitzer Strasse 40, D-01187 Dresden, Germany*⁴*SUPA, School of Physics and Astronomy and Centre for Science at Extreme Conditions, The University of Edinburgh, Edinburgh EH9 3FD, United Kingdom*⁵*Department of Materials Science & Metallurgy, University of Cambridge, 27 Charles Babbage Road, Cambridge CB3 0FS, United Kingdom* (Received 17 September 2022; revised 11 May 2023; accepted 19 August 2023; published 28 November 2023)

The charge-density-wave (CDW) amplitude mode of the high-pressure sulfur-IV phase is observed between 83 and 146 GPa using Raman spectroscopy. The energy of this excitation softens with pressure yet remains finite at $\nu_{\text{CDW}} > 100 \text{ cm}^{-1}$ up to the critical pressure, which is indicative of a weakly first-order transition. Our *ab initio* calculations show that the finite energy of the excitation originates from the coupling and mutual stabilization of the CDW modulation and a monoclinic lattice distortion. At the critical pressure, both the CDW modulation and lattice distortion disappear simultaneously. Due to the prevalence of CDW phases, this coupling between the CDW modulation and lattice distortion is expected to be relevant for a wide variety of elements and compounds.

DOI: [10.1103/PhysRevResearch.5.043188](https://doi.org/10.1103/PhysRevResearch.5.043188)**I. INTRODUCTION**

Charge density waves (CDWs) are modulations of electron density and atomic positions with a periodicity different from (and often incommensurate with) the underlying crystalline lattice [1]. CDWs are known to appear in a broad variety of materials where they can intrinsically cause metal-insulator transitions [2]. CDWs have so far been considered to be driven by nesting, electron-phonon coupling, excitonic mechanisms, or a combination thereof [1,3]. Here, we show that a CDW can also be tied to distortions of the underlying lattice at a wave vector other than the CDW periodicity. The coupling of the CDW to other order parameters (a lattice distortion in the present case of elemental sulfur) is not only important as part of the mechanism for the CDW, but it also alters the characteristics of the phase transition.

CDWs are known to form in eight elements, with seven of those at high pressures [4–21]. The pressure-induced onsets of the CDW phases are always first-order transitions, while the high-pressure transitions are ascribed to either first- or second-order transitions, often involving the extrapolation of structural or spectroscopic data [8,10,12–14,16,20,22]. If the CDW phase is a purely displacive structural phase transition

[23], a continuous decrease of the atomic displacement and a second-order transition to the higher-symmetry phase are expected. This argument has been used to characterize the suppression of the CDW phase in elemental sulfur [8]. Two distinct structural distortions corresponding to two order parameters have been measured with x-ray diffraction (XRD) in the sulfur-IV (S-IV) phase between 83 and 153 GPa [7,8]: the first is an incommensurate CDW with a finite wave vector ($q \neq 0$) and the other occurs at $q = 0$ and represents a monoclinic distortion to a body-centered-monoclinic (bcm) structure ($C2/m$) [5,6,24,25]. At lower pressures, the S-III phase is stable between 36 and 100 GPa with a body-centred-tetragonal ($I4_1/acd$) structure [5,6,26]. At higher pressures, the S-V phase is stable above 153 GPa with a rhombohedral β -Po ($R\bar{3}m$) structure [6,8]. The first-order nature of the transition from S-III to S-IV is well established with a coexistence region between 83 and 100 GPa. However, we demonstrate that the characterization of the S-IV to S-V transition is more subtle than previously thought and is tied to the interplay of the two order parameters and the mechanism of the CDW.

We use Raman spectroscopy to directly measure the CDW amplitude mode. This amplitude mode is a robust signature of a CDW and is always Raman active [27]. This has resulted in it being observed in many CDW systems [28], including in other elemental systems, i.e., selenium and tellurium [22,29]. However, the CDW mode in these elements could not be followed conclusively to the phase boundary and the mechanism of the CDW has not yet been established.

We follow the CDW amplitude mode throughout sulfur S-IV. Surprisingly, the amplitude mode retains a finite energy at the critical pressure of the CDW. We reproduce this behavior with *ab initio* density functional theory (DFT) calculations,

*owen.moulding@neel.cnrs.fr

†sven.friedemann@bristol.ac.uk

Published by the American Physical Society under the terms of the [Creative Commons Attribution 4.0 International](https://creativecommons.org/licenses/by/4.0/) license. Further distribution of this work must maintain attribution to the author(s) and the published article's title, journal citation, and DOI.

and we show that this is evidence for coupling between the incommensurate CDW modulation (approximated by a commensurate $q = 3/4$ wave vector) and a monoclinic lattice distortion ($q = 0$), which are simultaneously suppressed with increasing pressure. The coupling of the modulation and distortion drives weakly first-order behavior at the S-IV to S-V phase transition.

II. METHODS

High-pressure experiments were performed using three diamond anvil cells: SIO1, SOM9, and SIO3. Data from SIO1 is presented in the main text, while data from SOM9 and SIO3 are presented in Appendix A. All the diamonds used here had culet diameters of 50 μm and single bevels with diameters of 300 μm . SIO1 and SIO3 used type-2A low-fluorescence Boehler diamonds, which minimized the background in these Raman measurements, whereas SOM9 used type-1A brilliant-cut diamonds. Gaskets were made from 250- μm -thick T301 steel pre-indented to approximately 20 μm . A 200 μm circle was removed with a laser cutter, which was then replaced by a layer of hardened stycast 2850FT and boron-nitride mixture that was indented at 30 GPa. Finally, a 30 μm hole was removed with a laser cutter to form the sample space.

Three samples were prepared by flattening sulfur (99.5%, Alfa Aesar) to approximately 3 μm thick and then cut by hand into approximately $25 \times 25 \mu\text{m}^2$ squares (an example is shown in Appendix A). The sample chamber was loaded with ammonia borane, which acted as a quasi-hydrostatic pressure medium. At the pressures of interest, ammonia borane has no sharp Raman excitations and acts as a background contribution in the same way as the diamond anvils. However, we suspect it causes the feature at 500 cm^{-1} .

Micro-Raman spectroscopy was performed in a backscattering geometry with a 532 nm solid-state laser. The scattered light was filtered by a RazorEdge ultrasteep long-pass edge filter to achieve a low-energy cutoff of 100 cm^{-1} , which removed the Rayleigh scattered light and laser contributions. The scattered light was collected by a Horiba Scientific iHR320 spectrometer equipped with a Horiba Scientific Sincerity deep-cooled CCD and a single-stage grating (1800 gr/mm). In such a configuration, the resolution is approximately 3 cm^{-1} . All spectra were obtained at room temperature (≈ 293 K) and with increasing pressure. The pressure was determined from the high-frequency edge of diamond [30], and some examples are shown in Appendix A. The peaks in all the sulfur spectra were fitted with Lorentzians once a background contribution was subtracted (see Appendix A). All excitations are identified by their symmetries and whether they are stretching (s) or bending (b) modes, as determined by our calculations.

DFT calculations with the CASTEP and QUANTUMESPRESSO software packages [31,32] were used to compute the energetics, structural trends, and lattice dynamics of the S-III, S-IV, and S-V phases, as detailed in Appendix B. To model the incommensurate CDW within the S-IV phase, an 8-atom $1 \times 4 \times 1$ supercell of the bcm structure was used, which is itself a monoclinically distorted twofold supercell of the monatomic S-V (β -Po) structure [33]; hence, the 8-atom supercell can accommodate both the CDW modulation and a monoclinic

distortion. The CDW is approximated by a commensurate modulation of $q = 3/4(2\pi/b) = 1.359 \text{ \AA}^{-1}$, which is within 0.5% of the experimentally observed incommensurate q vector of 1.365 \AA^{-1} [7]. Potential-energy surfaces were obtained by independently varying the CDW amplitude and monoclinic distortion between the CDW approximant structure and the S-V structure.

III. RESULTS

The pure S-III phase exists between 36 and 83 GPa [5]; within this region, five phonon modes out of an expected seven are observed in our Raman measurements, as shown in Figs. 1(a) and 1(b). The energies of these modes continue to increase with increasing pressure and they persist throughout the coexistence region of the S-III and S-IV phases up to 95 GPa [8]. All modes in the S-III phase are in good quantitative and very good qualitative agreement with our calculations.

Three excitations that agree with the theoretical predictions for the S-IV phase emerge within the S-III/S-IV coexistence region. These also persist into the pure S-IV phase and disappear in the S-V phase, in agreement with earlier reports [34]. Two of these excitations (A_g and B_g) are associated with lattice modes of the S-IV phase and occur at approximately 350 and 400 cm^{-1} , respectively. The A_g mode is very close in energy to the S-III E_g^{b2} mode, though they are distinct modes, as described by their symmetries. Indeed, this continuity is consistent with calculations which show that the E_g^{b2} mode present within the S-III phase is comparable in energy to the A_g mode present throughout the S-IV phase. The B_g mode at 400 cm^{-1} also agrees well with theoretical calculations.

The spectral weights of the A_g and B_g phonon modes trace the emergence and suppression of the CDW, as shown in Fig. 1(c). The initial increase in spectral weight below 104 GPa is interpreted as an increase of the S-IV volume fraction within the coexistence region that reaches 100% at 104 GPa. The decrease of spectral weight above 104 GPa is related to the reduction of the CDW displacement [7]. As the A_g and B_g modes are CDW folded acoustic modes of the single-atom S-V unit cell (see Appendix B), their existence is intrinsically linked to the strength of the CDW modulation and their spectral weight is indeed expected to scale with the CDW displacement.

We identify the lowest-energy Raman excitation with an energy of 150 cm^{-1} in the S-IV phase as the CDW amplitude mode. This low-energy excitation emerges in the S-III/S-IV coexistence region and it persists throughout the pure S-IV phase before disappearing at the S-V phase boundary. Thus this excitation is uniquely associated with the S-IV phase. The $\approx 150 \text{ cm}^{-1}$ mode is the only experimentally observed excitation to soften with pressure [Fig. 1(b)], which is naturally associated with the suppression of the CDW modulation [7]. Indeed, our DFT calculations below support this, as the predicted energy of the CDW amplitude mode agrees remarkably well with experiment. The increasing intensity below 104 GPa reflects the increasing volume fraction of S-IV in the coexistence region exactly the same way as for the A_g and B_g modes. The decreasing intensity above 104 GPa highlights that the $\approx 150 \text{ cm}^{-1}$ mode is indeed tied to the CDW. The spectral

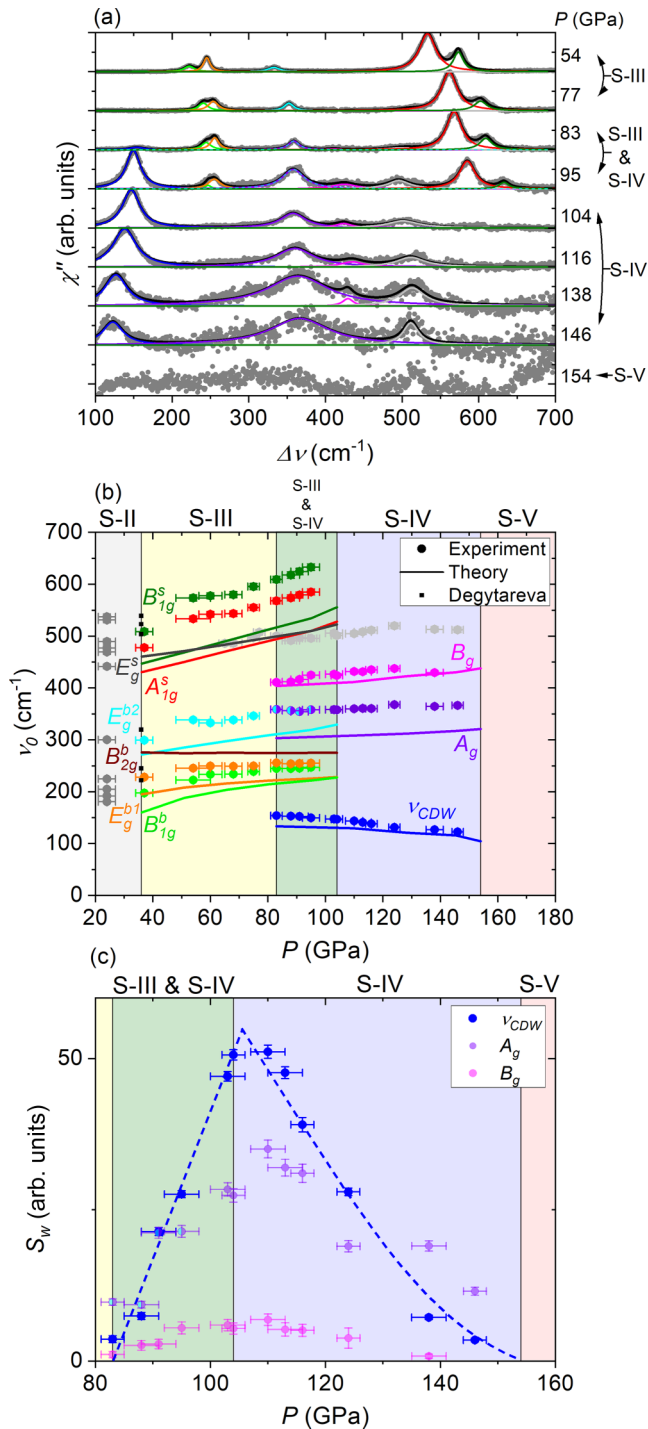


FIG. 1. (a) Raman spectra of sulfur between 55 and 154 GPa normalized to the maximum intensity at a given pressure. Solid colored lines are fits to the individual excitations. Solid black lines correspond to the total fitted spectra. (b) Experimental (symbols) and calculated (lines) energies of Raman-active excitations labeled according to the symmetries identified in DFT calculations and whether they are stretching (s) or bending (b) modes. The five known characteristic regions in the studied pressure range are labeled and indicated by background color. The pressures determined from DFT calculations have been linearly scaled (see Appendix D). (c) The unnormalized spectral weights of the excitations associated with the S-IV phase. The dashed line is a guide to the eye showing the evolution of the CDW excitation.

weight decreases continuously with pressure before disappearing completely at the S-V phase boundary at 153 GPa [7].

The central result of our measurements is that the energy of the CDW amplitude mode remains finite up until the S-V phase boundary, while the spectral weight of the CDW mode is fully suppressed [Figs. 1(b) and 1(c)]. The finite energy of the CDW amplitude mode implies a discrete energy change at the S-IV to S-V phase boundary as the CDW becomes unstable, which suggests a weakly first-order transition at the critical pressure of the CDW. Below, we show in our DFT calculations that a weakly first-order transition arises as a result of the coupling between the CDW modulation and monoclinic distortion and their simultaneous removal at the phase boundary.

We find all the experimentally observed high-pressure phases of sulfur to be sequentially stable in our *ab initio* calculations. The transition pressures of S-III to S-IV, and S-IV to S-V, are $P_{\text{DFT}} = 66$ and 77 GPa, respectively (see Appendix D), where P_{DFT} refers to pressures extracted from our DFT calculations. Though these calculated pressures are lower than seen in experiment, they are in agreement with previous calculations [35]. We use a linear scaling calculated from the experimentally determined phase boundaries to scale P_{DFT} onto the experimental pressures (see Appendix D). In S-III, the calculated pressure-dependent energies of the seven Raman-active phonon modes are found to be in good agreement with experiment (see Appendix C). The calculations also show a hardening of all modes close to what is experimentally observed and hence validate the use of the pressure scaling between DFT and experiment.

The CDW amplitude mode identified in our DFT calculations with $q = 3/4$ is in excellent agreement with experiment, as we very closely reproduce the energy and the characteristic softening. Most importantly, our DFT calculations show that the energy of the CDW amplitude mode remains above 100 cm^{-1} up to the critical pressure of the CDW, before disappearing when the CDW ceases to exist. The sudden disappearance of the CDW excitation can be explained by our calculations when considering the energy landscape around the S-IV to S-V transition. A key insight is that S-IV can be understood in terms of a monoclinic distortion of the S-V lattice (a perturbation with wave vector $q = 0$) alongside the CDW modulation ($q = 3/4$). Figure 2 illustrates that in the S-IV phase, both the monoclinic distortion and the CDW modulation are independently higher in enthalpy than S-V; only together do they result in the stable energetic minimum of $P2_1/m$ S-IV, where $P2_1/m$ is the symmetry of the approximant of the incommensurate CDW phase. Hence we conclude that the CDW and monoclinic distortion mutually stabilize one another. Another way of viewing the same phenomenon is that the atomic bonds are affected by two independent symmetry-breaking operations caused by the monoclinic lattice distortion and the CDW modulation (indicated in Fig. 2 by the color of the bonds). Without the effects of the CDW modulation and lattice distortion, there is only one type of bond (fully symmetric $R\bar{3}m$, blue); however, this changes with the introduction of the lattice distortion (red) and CDW modulation (yellow, green, purple). This dual symmetry breaking of S-V is what gives rise to the weakly first-order behavior that is observed at the S-IV/S-V phase boundary.

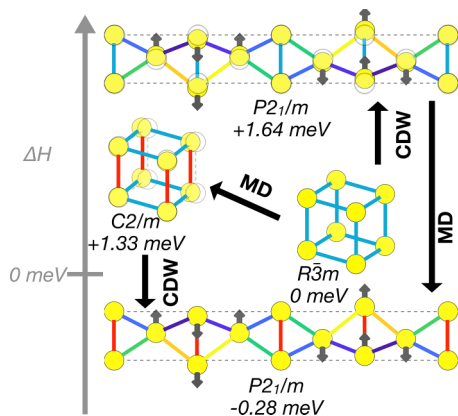


FIG. 2. Crystal structures of sulfur and their enthalpy difference per atom, relative to the S-V $R\bar{3}m$ structure at $P_{\text{DFT}} = 70$ GPa, which corresponds to an experimental pressure of 129 GPa and is within S-IV. Bonds are colored to indicate symmetrically equivalent bonds. Arrows show the direction of displacement of the atoms in the CDW. Shaded atoms show the S-V structure. Atomic displacements are exaggerated for visibility. The difference between the $P2_1/m$ structure with and without the monoclinic distortion (MD) is visible from the nonequivalent bonds.

Our DFT calculations show that this mutual stabilization exists throughout S-IV and persists until the upper critical pressure of the CDW. Figure 3 shows the potential enthalpy surface of the S-IV approximant as functions of the magnitudes of the CDW amplitude (x axis) and monoclinic lattice distortion (y axis). Consequently, S-V is located at $(0,0)$, labeled with $R\bar{3}m$, since there is no monoclinic distortion or CDW present, while the S-IV approximant ($P2_1/m$) is at $(\approx \pm 0.05, \approx 0.9)$ with a finite CDW amplitude and lattice distortion. At $P_{\text{DFT}} = 70$ GPa, S-IV is the global minimum, while S-V is barely a local minimum, which can be seen by the gradient lines. At $P_{\text{DFT}} = 75$ GPa, both the S-IV and S-V structures are minima, while at $P_{\text{DFT}} = 80$ GPa, all structures relax directly to the S-V structure. Above $P_{\text{DFT}} = 77$ GPa, as determined from enthalpy calculations in Appendix D, there

is a clear energetic pathway for S-IV to transition to S-V by simultaneously reducing the CDW amplitude and lattice distortion to zero, which results in the high-symmetry $R\bar{3}m$ structure. We propose that this simultaneous disappearance of these two independent symmetry-breaking effects gives rise to weakly first-order behavior, which also manifests itself as the experimentally observable disappearance of the CDW excitation.

IV. DISCUSSION AND CONCLUSIONS

Previous XRD measurements in sulfur have shown that the volume discontinuity at the S-IV/S-V phase boundary is negligible, which suggests a second-order transition [6,8,24]. Our calculations predict a negligible volume discontinuity as the monoclinic distortion from $R\bar{3}m$ causes a small volume change of 0.1% at $P_{\text{DFT}} = 75$ GPa. This small volume change is also accompanied by a small energetic barrier between the S-IV and S-V structures at the transition pressure (≈ 0.1 meV/atom), which would easily be overcome by thermal energy at room temperature. Thus a coexistence region is not expected to be present at room temperature, though this cannot be confirmed here as the S-V phase has no Raman-active modes. Since our calculations reproduce well-known characteristics of second-order phase transitions while simultaneously predicting a sudden disappearance of the CDW excitation, it seems that the coupling and subsequent suppression of the two order parameters corresponding to the CDW modulation and lattice distortion give rise to emergent weakly first-order behavior in S-IV.

Our study establishes a different mechanism for CDWs: The coupling of the CDW and monoclinic distortion stabilizes both of these structural features. Such a coupling may also be relevant for the stability of the CDW in selenium and tellurium and may be identified through extended Raman studies to higher pressures and lower energies than possible to date [22,29]. More broadly, a coupling between the CDW and other phases may play a role in the understanding of unconventional CDWs, such as in CsV_3Sb_5 and NbSe_3 , where multiple CDWs are observed with the lower transition potentially terminating

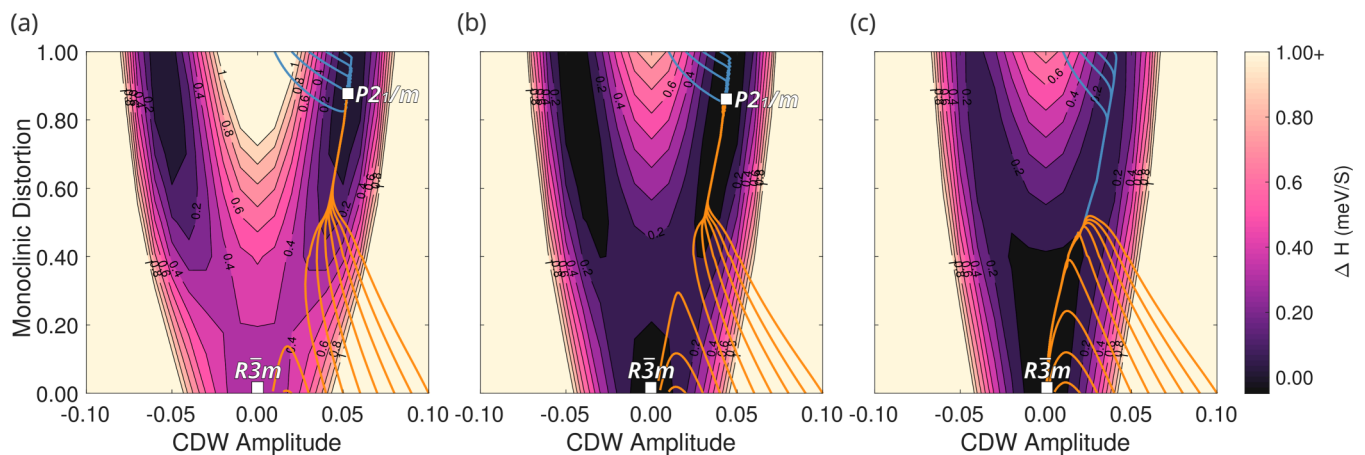


FIG. 3. Contour plots of potential enthalpy surfaces at $P_{\text{DFT}} = 70, 75,$ and 80 GPa around the S-V (at $x = 0, y = 0$) and S-IV (at $x \approx \pm 0.05, y \approx 0.9$) modulated bcm structures. Enthalpy contours are relative to the global minimum in meV/atom. Enthalpies above 1 meV/atom are saturated on this scale. Orange gradient lines begin at $y = 0$ and blue gradient lines begin at $y = 1$.

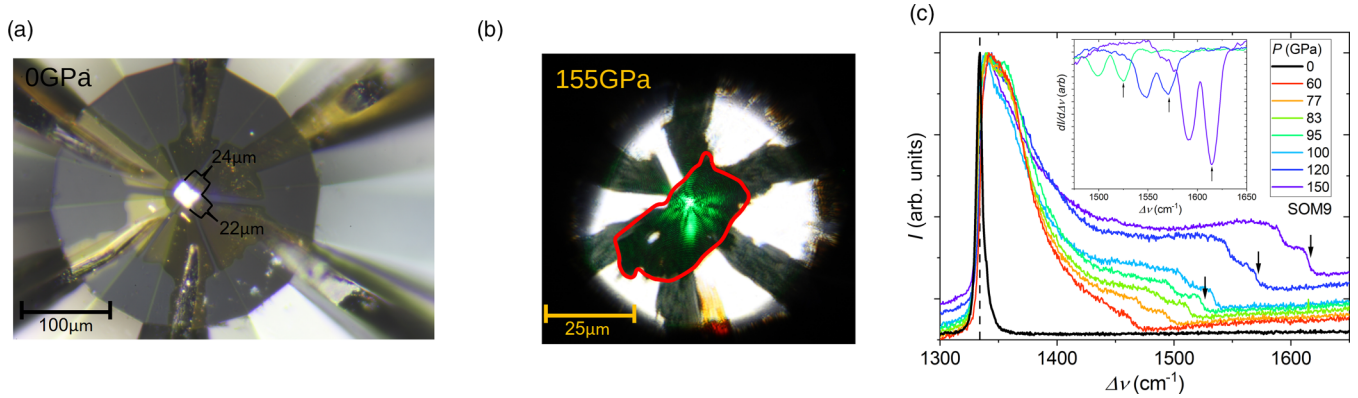


FIG. 4. (a) Ambient pressure sulfur sample on the 50 μm culet with electrodes for transport measurements. (b) The same sulfur sample (outlined in red) at 155 GPa with the laser incident on the center of the sample and culet. The applied pressure caused the sulfur to extrude. (c) Spectra of the diamond phonon under pressure from SOM9. In black is the ambient pressure diamond phonon at 1334 cm^{-1} ; high-pressure spectra have been normalized to the intensity of the ambient pressure phonon. The high-frequency edge of the diamond is indicated by black arrows and corresponds to a minimum in the derivative (as shown in the inset).

in a first-order transition [36,37]. The concepts of coupled order parameters developed in the present work may also help one to understand the emergence of superconductivity observed near CDW transitions, such as in the cuprates [38–40] and transition-metal chalcogenides [41–44]. In cuprates, the complex phase diagram features many charge and spin orders that may give rise to coupled order parameters. The change to first order also highlights that coupled order parameters can be relevant for a Landau free-energy expansion [45–47], which in CDW systems often gives rise to new phenomena as both order parameters can give rise to fluctuations [48].

Data are available at the University of Bristol data repository at Ref. [49].

ACKNOWLEDGMENTS

The authors thank M.-A. Méasson for valuable discussions. The authors acknowledge the support of EPSRC Grants No. EP/R011141/1, No. EP/L025736/1, No. EP/N026691/1, No. EP/L015110/1, and No. EP/S021981/1, as well as the ERC Horizon 2020 programme under Grant No. 715262-HPSuper. Computational resources provided by the UK’s National Supercomputer Service through the UK Car-Parrinello consortium (Grant No. EP/P022561/1) and by the UK Materials and Molecular Modeling Hub (Grant No. EP/P020194) are gratefully acknowledged.

S.F., J.B., and O.M. initiated this project. O.M. and I.O. prepared the pressure cells and carried out the Raman measurements. J.B. constructed the Raman setup and supervised Raman measurements and data analyses, along with S.F. In addition, L.J.C. and A.H. performed the theoretical calculations. O.M. and L.J.C. wrote the manuscript with input from all the other co-authors.

The authors declare no competing interests.

APPENDIX A: SPECTRAL ANALYSIS, SOM9, AND SIO3

Figure 4(a) shows a photo of a prepared pressure prior to closing with the sulfur sample in place on the culet of

the diamond. Similarly, Fig. 4(b) shows a photo of the same sample but after applying 155 GPa of pressure, which caused the sample to extrude.

Figure 4(c) shows typical Raman spectra of diamond under high pressure. At ambient pressure, there is a phonon at 1334 cm^{-1} ; at higher pressure, the phonon hardens and broadens considerably. As indicated by the black arrows, there is a noticeable shoulder which corresponds to the high-frequency edge of the diamond. By taking the derivative, one sees that this shoulder corresponds to a minimum (as shown in the inset). Since it is a strong feature as a function of pressure, the energy at which the minimum occurs is used as a pressure gauge [30]. The uncertainty in the pressure is estimated from the full width at half maximum, and this is reliably of the order of ± 5 GPa.

To analyze the spectra, several steps were used to process the data; some examples of raw spectra from SIO1 are presented in Fig. 5(a). First, a constant background contribution from the spectrometer was subtracted before the spectra were scaled by the incident laser power (0.6 mW) and the exposure time (generally 15 mins). Next, the spectra (I_0) were corrected for the Bose factor to obtain the Raman response,

$$\chi'' = I_0(1 - e^{-\frac{hc\Delta\nu}{k_B T}}), \quad (\text{A1})$$

which accounts for thermal occupation as a function of Raman shift ($\Delta\nu$). Next, a background was subtracted from the spectra to yield the pure excitations of sulfur. For SOM9, the spectra were taken on and off the sample and scaled such that the spectra overlapped; the off-sample spectra were then subtracted from the on-sample spectra. This yielded the spectra shown in Fig. 5(b). For SIO1 and SIO3, a parabola was fitted to the background and subtracted to yield the spectra shown in the main text and in Fig. 5(c), respectively. Both analyses yielded similar results, as shown in Figs. 5(d) and 5(e).

As shown in Fig. 1(b), the E_g^s mode is predicted to be close in energy to the A_{1g}^s and B_{1g}^s modes over a broad pressure range. We use SIO3 to distinguish a third weak mode that we associate with the E_g^s mode. Within the S-III phase at 53 GPa and with the aid of polarizers, we can identify a third weak

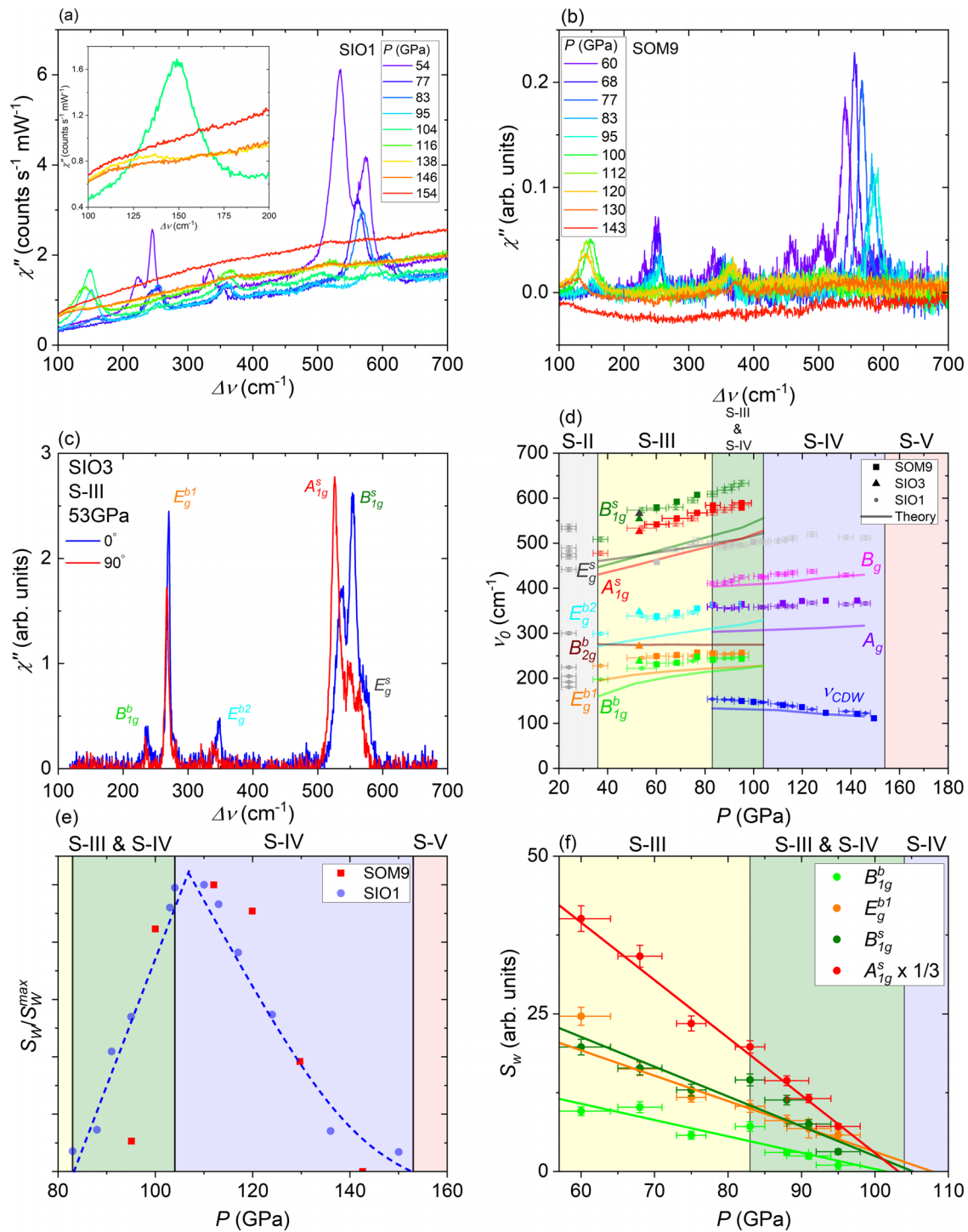


FIG. 5. (a) Data from SIO1 across the measured pressure range without background subtraction. Inset: The region demonstrating the large suppression of the CDW amplitude mode from where it is most intense at 104 to 154 GPa, where the excitation has been completely suppressed. (b) Background-subtracted spectra from SOM9. (c) Background-subtracted spectra from SIO3 within the S-III phase at 53 GPa. Two polarizers are used in parallel (0°) and perpendicular (90°) orientations. The modes are labeled with the symmetry allocations of the main text. In these spectra, the E_g^s mode is visible as a weak shoulder. (d) Peak energies vs pressure for all three sulfur samples and compared to calculations. Data from SIO1 and calculations (shown in main text) are faded to emphasize the data from SOM9 and SIO3. (e) Normalized S_W of the CDW excitation as a function of pressure for SIO1 and SOM9. (f) The unnormalized spectral weights (S_W) of the modes purely associated with the S-III phase from SIO1. Solid lines are linear fits to the data, with the x intercept giving the upper critical pressure of the S-III/S-IV coexistence region as 104 ± 7 GPa.

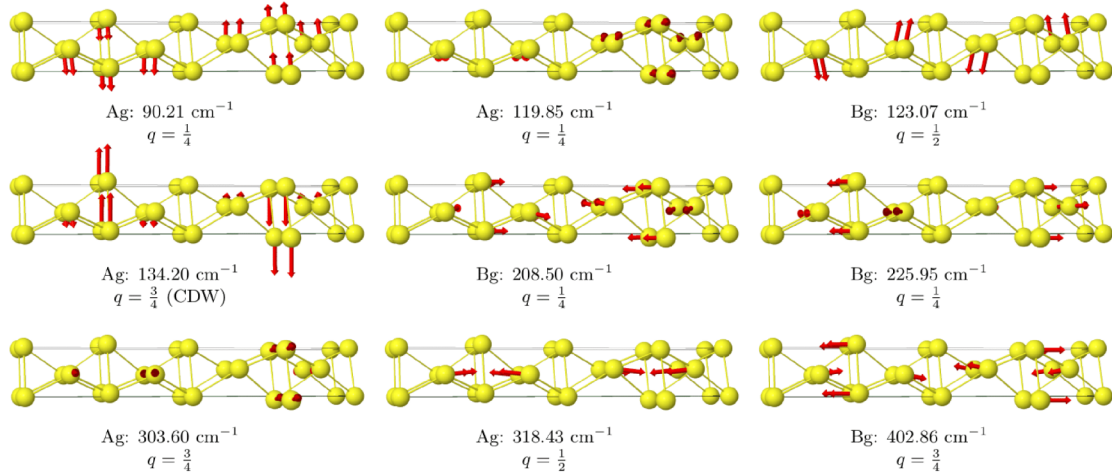


FIG. 6. Calculated displacement vectors of the Raman-active modes at $P_{\text{DFT}} = 60$ GPa for S-IV in the $q = 3/4$ approximation. The effective wave vector of each displacement vector is given.

mode, which is shown in Fig. 5(c), that could not be observed in the unpolarized measurements of SIO1 and SOM9. At this pressure, the B_{1g}^s and E_g^s modes have very similar energies as predicted by DFT calculations, as this pressure approximately corresponds to a crossing point in energy, i.e., above this pressure, the B_{1g}^s mode becomes the highest-energy mode. A consequence of this is that the E_g^s mode becomes flanked by two strong modes, which makes it more challenging to measure above this pressure where the majority of the data in SIO1 are measured.

The B_{2g}^b mode was neither observed by us nor previously in agreement with the very low intensity predicted for this mode

(see Appendix C). A final weak mode (light gray) appears within the S-III phase, though we believe that it is an artifact of the ammonia borane pressure medium.

Figure 5(d) shows the peak energies for all three sulfur samples alongside predictions and show that all the samples agree very well. Figure 5(e) shows the normalized spectral weight of the CDW excitation for SIO1 and SOM9, and both samples show a similar qualitative trend with pressure, i.e., a large enhancement within the coexistence region followed by suppression as the S-V phase is approached.

Beyond the coexistence region of the S-III and S-IV phases exists the pure S-IV phase, which is clearly marked by the

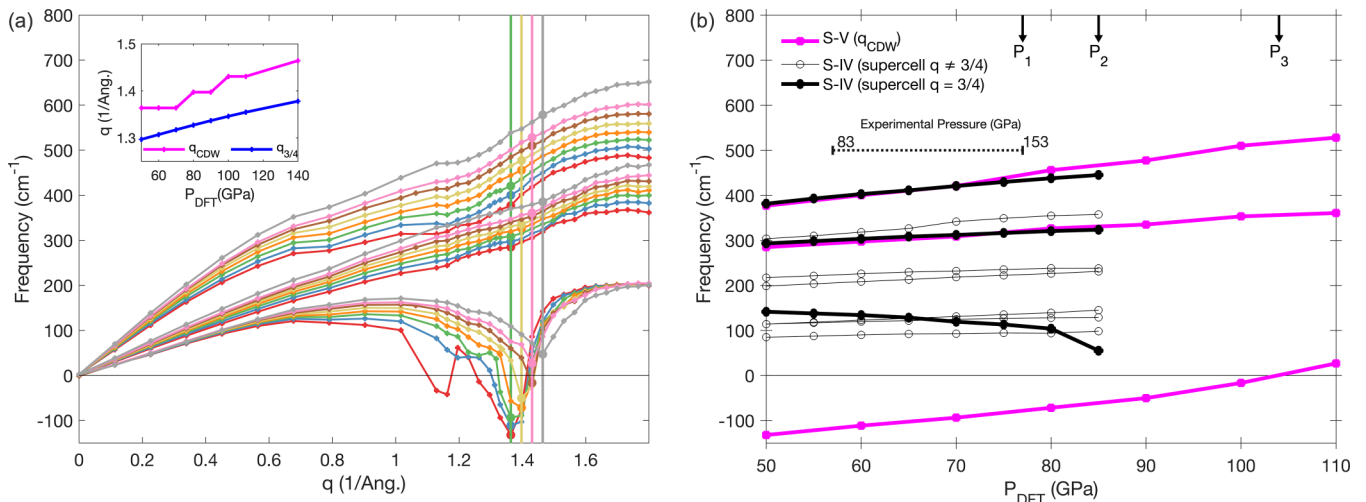


FIG. 7. (a) Calculated phonon dispersion of the S-V structure along the [100] direction. Colors correspond to different pressures, in steps of 10 GPa from $P_{\text{DFT}} = 50$ GPa (red) to 110 GPa (pink), and $P_{\text{DFT}} = 140$ GPa (gray). Vertical lines represent the q_{CDW} vector with the minimum in the phonon instability toward the CDW S-IV structure. The frequencies of the two positive branches at q_{CDW} are used to estimate S-IV modes. (b) Calculated Raman-active modes for S-IV using S-V dispersions (magenta) and using the commensurate approximation supercells (black). Open black symbols are Raman-active modes that are unlikely to appear in a real incommensurate structure because they either result from back-folding or are above P_1 , the pressure at which the unmodulated structure becomes the global minimum. Filled black symbols are modes associated with the $q = 3/4$ CDW approximation. P_2 is the pressure at which the modulated structure is no longer dynamically stable. P_3 is the pressure at which the $R\bar{3}m$ structure has only stable phonon modes. The dashed horizontal line shows the pressure scale used for comparison to experimental measurements.

disappearance of four phonon modes purely associated with the S-III phase. Figure 5(f) shows that the spectral weights (S_W) of the B_{1g}^b , E_g^{b1} , B_{1g}^s , and A_{1g}^s modes diminish until they are all completely suppressed at 104 ± 7 GPa, which coincides with the end of the coexistence region as determined by previous XRD measurements [5–8,24–26]. This diminishing is associated with the decreasing volume fraction of the S-III phase. Most notably, the A_{1g}^s mode is consistently the most intense mode within the S-III phase and its disappearance is a clear indication of the complete structural transformation.

APPENDIX B: S-IV AND S-V PHONON CALCULATIONS

DFT calculations were done using the CASTEP and QUANTUMESPRESSO software packages [31,32]. Specifically, CASTEP was used to determine enthalpies for all phases; the pressure dependence of the S-IV Raman mode energies and the S-III Raman intensities were determined using density functional perturbation theory. QUANTUMESPRESSO was used to compare values to the literature.

We calculated the Raman-active modes of the approximated commensurate S-IV CDW structure using an 8-atom supercell which possesses nine Raman-active modes. Figure 6 shows the approximate S-IV structure with the displacement vectors of the modes alongside their symmetries and energies (at $P_{\text{DFT}} = 60$ GPa). Examination of the eigenvectors reveals that only three modes actually correspond to a $q = 3/4$ wave vector. The remaining modes correspond to $q = 1/4$ or $q = 1/2$ and are therefore a consequence of the supercell construction and not truly zone-centered modes. Since these modes are a consequence of the $q = 3/4$ approximation of an incommensurate structure, they are not physical and can be ignored. The three $q = 3/4$ modes agree well with experiment and are shown in Fig. 1(b). In particular, a low-energy mode that softens with pressure is found to be a consequence of the CDW.

Figure 7(a) shows the calculated phonon dispersion of S-V. The CDW wave vector is measured at the minimum of the phonon instability and differs from the absolute value of $q = 3/4$ (see inset). If the phonon instability is used to indicate the stability region of S-V, the high-pressure transition can be calculated to be 105 GPa. A similar calculation appears in Ref. [7], which suggests a calculated transition of 130 GPa. However, we find that the difference in critical pressures can result from an insufficient sampling of the Brillouin zone. A comparison of these calculations at 50, 100, and 130 GPa is shown in Fig. 8. At 130 GPa, an electronic k -point grid of $16 \times 16 \times 16$ (as used in Ref. [7]) gives a phonon instability which is not seen when calculations are performed on a $28 \times 28 \times 28$ or denser grid.

Calculations of S-V and S-IV structures are therefore highly sensitive to Brillouin zone sampling. This is also shown in a recent theoretical study of the sulfur system [35], which suggests a transition from the S-IV modulated bcm structure to an unmodulated bcm structure with $C2/m$ space group and a 0.002 \AA lattice distortion from the S-V $R\bar{3}m$ structure at around 100 GPa. We find that this lattice distortion is dependent on the chosen k -point grid; modeling the monatomic $R\bar{3}m$ primitive cell with a $48 \times 48 \times 48$ grid gives the $R\bar{3}m$ structure as the ground state, while modeling it with a $48 \times 48 \times 49$ grid gives rise to the distortion and the $C2/m$

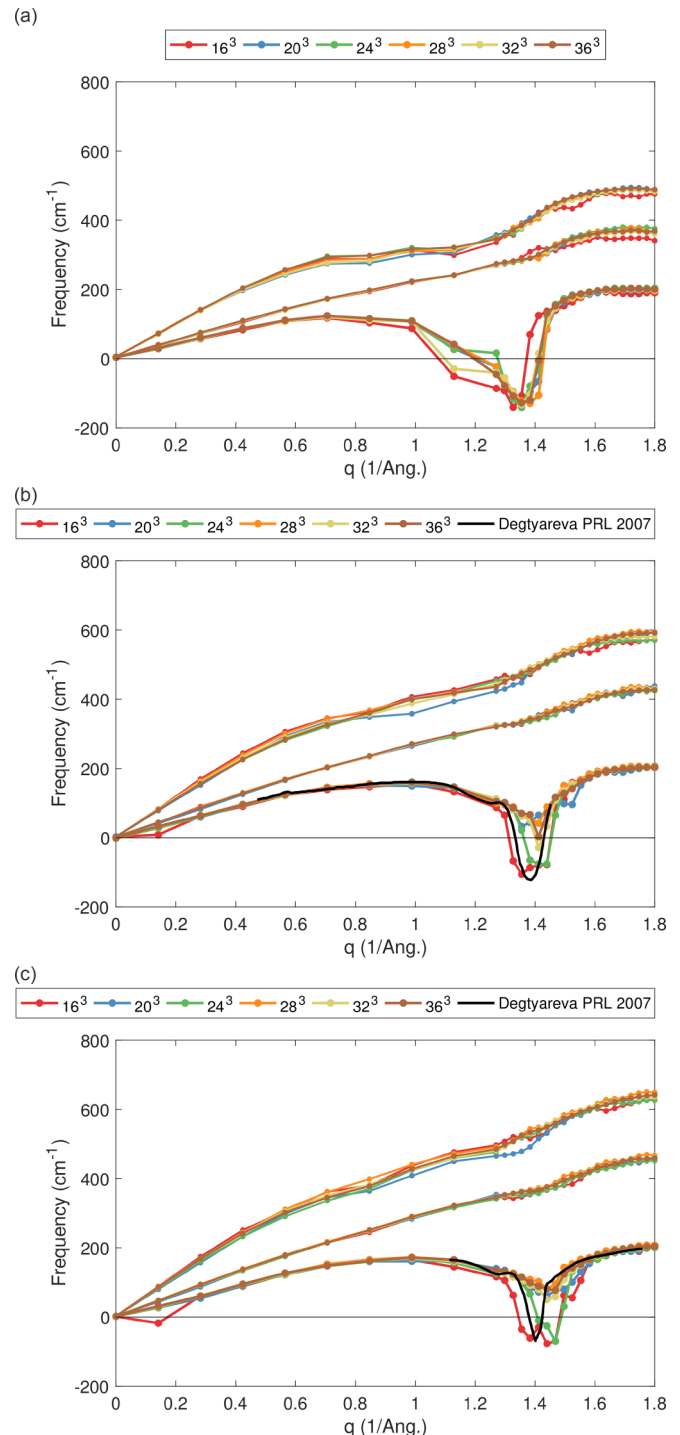


FIG. 8. Phonon-dispersion curves at (a) 50 GPa, (b) 100 GPa, and (c) 130 GPa with varying electronic k -point grids compared to previous DFT calculations from Ref. [7].

structure. Both structures have a similar k -point spacing of $0.01 \times 2\pi/b \text{ \AA}$.

Figure 7(b) shows the Raman frequencies of the 8-atom S-IV approximant alongside the folded S-V structure with q_{CDW} determined from the minimum of the phonon dispersion in the inset of Fig. 7(a). Open symbols show the frequencies expected for $q \neq 3/4$ modes including pressures above P_1 , which corresponds to the unmodulated structure becoming the

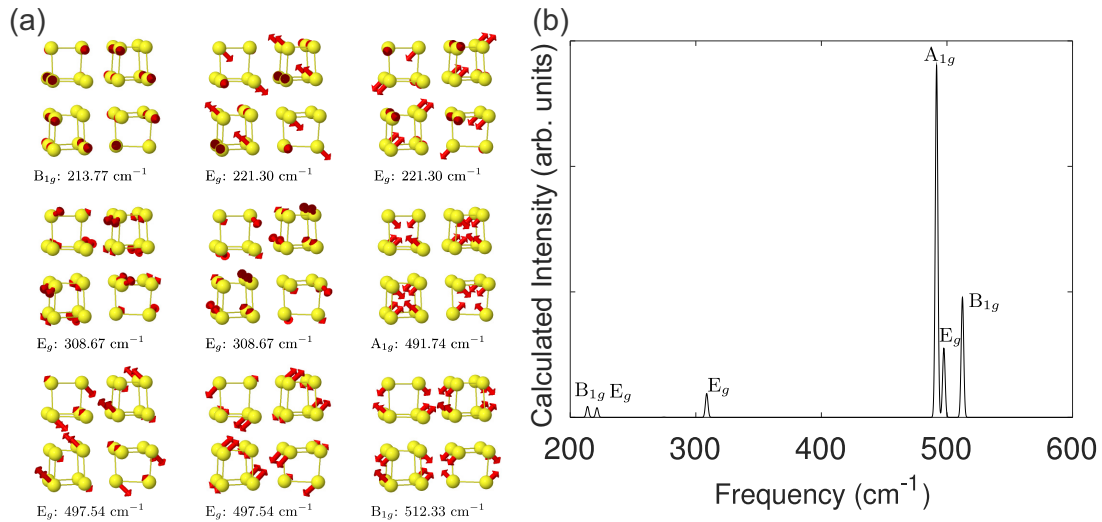


FIG. 9. (a) Calculated displacement vectors of the Raman-active modes at $P_{\text{DFT}} = 50$ GPa for S-III. (b) Calculated Raman intensities for S-III at $P_{\text{DFT}} = 50$ GPa. The E_g modes are doubly degenerate.

global enthalpy minimum. Excellent agreement is found between the calculated approximant structure ($q = 3/4$) and the acoustic phonon modes of the S-V structure at the minimum of the softening phonon, as shown by the agreement between the black and magenta data.

To generate the potential enthalpy surfaces, the atoms were displaced from the high-symmetry sites by a modulation wave given by

$$\delta \mathbf{r} = x \mathbf{a} \sin(6\pi r_b), \quad (\text{B1})$$

where x is the amplitude of the displacement, \mathbf{a} is the displacement vector of either the CDW or the monoclinic distortion, and r_b is the fractional coordinate along the b axis. Varying the value of x between -0.1 and 0.1 probes the energy landscape along the CDW perturbation. Similarly, the monoclinic distortion was varied by linearly interpolating the lattice parameters

between the rhombohedral ($y = 0$) and monoclinic ($y = 1$) structures.

APPENDIX C: S-III RAMAN CALCULATIONS

Figure 9 shows the structure of S-III alongside the displacement vectors of each predicted mode, the symmetry, and the energy of the mode at $P_{\text{DFT}} = 50$ GPa. Due to S-III being insulating, it is possible to calculate the Raman intensities of the excitations, which are shown in Fig. 9(b). At this pressure, the high-energy E_g mode (E_g^s from main text) lies between two stronger modes. Figure 10 shows the unscaled pressure dependence of the calculated S-III Raman-active modes, whereas Fig. 1(b) shows the scaled pressure dependence. The relative size of the points corresponds to the predicted intensity of

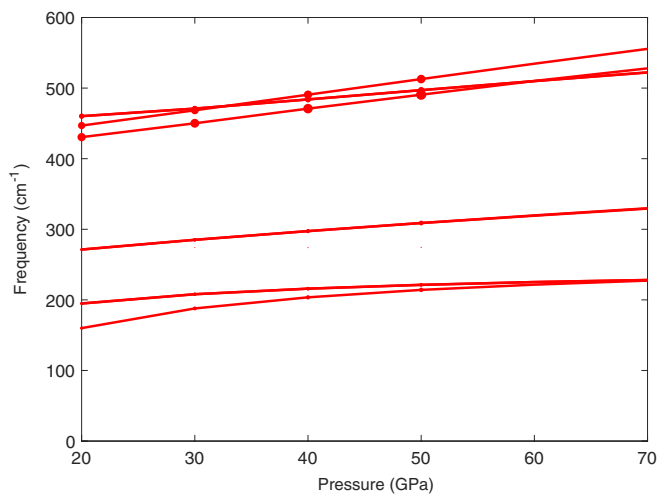


FIG. 10. Calculated Raman-active modes for S-III. Symbol size corresponds to calculated mode intensity.

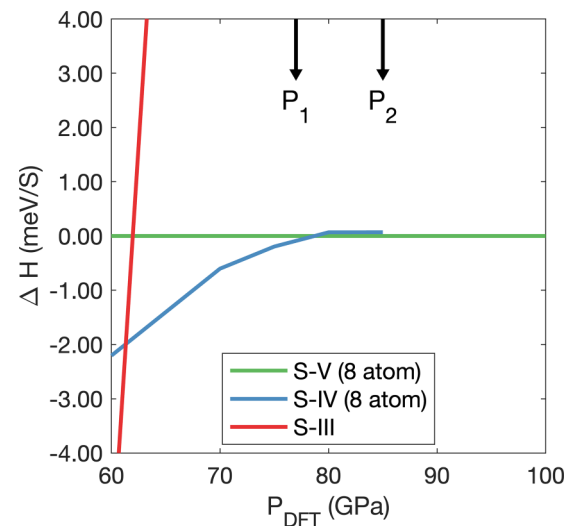


FIG. 11. Enthalpy plot of competing sulfur phases. The S-IV line ends when the CDW can no longer be stabilized in geometry optimization.

TABLE I. The parameters used to linearly scale the calculated P_{DFT} values to experimental P_{Expt} values by using experimental and predicted phase boundaries.

| | $P_{\text{Expt}}^{\text{lower}}$ (GPa) | $P_{\text{Expt}}^{\text{higher}}$ (GPa) | $P_{\text{DFT}}^{\text{lower}}$ (GPa) | $P_{\text{DFT}}^{\text{higher}}$ (GPa) | a (GPa) | b |
|-------|--|---|---------------------------------------|--|-----------|-----|
| S-III | 36 [5,6,26] | 104 | 20 | 66 | 6.4 | 1.5 |
| S-IV | 83 [7,8] | 153 [7,8] | 57 | 77 | -139 | 3.9 |

a given mode. The B_{2g} is not shown as it is predicted to be 0.06% of the intensity of the largest peak.

APPENDIX D: TRANSITION PRESSURES AND PRESSURE SCALING

Figure 11 shows the calculated enthalpies of the S-III, S-IV (8-atom), and S-V (8-atom supercell) structures with transition pressures of $P_{\text{DFT}} = 66$ and $P_{\text{DFT}} = 77$ GPa for S-III to S-IV, and S-IV to S-V, respectively. One phonon frequency of the S-V structure is imaginary, which indicates an energetic preference of S-IV over a wider pressure range up to $P_{\text{DFT}} = 105$ GPa. All of these calculated pressures are lower than seen

in experiment, but in agreement with previous calculations [35]. In our enthalpy calculations, we use the 8-atom supercells of S-IV and S-V with the same dense k -point spacing (see Appendix B). In these calculations, the atomic positions and lattice shape were fixed and only the volume was allowed to change to equilibrate with pressure.

As discussed in the main text, the S-IV to S-V transition occurs partly by a lattice distortion which is not captured in the S-V phonon dispersion calculations, so we use $P_{\text{DFT}}=77$ GPa from the enthalpy data. However, the predicted transitions clearly underestimate the experimentally confirmed transition pressures. To aid comparison between the experimentally observed and theoretically calculated transition pressures for the S-III and S-IV phases, a linear transformation given by

$$P_{\text{Expt}} = a + bP_{\text{DFT}} \quad (\text{D1})$$

was used to scale the calculated pressure dependencies. By solving Eq. (D1) with the known experimental phase boundaries taken from the literature and the phase boundaries predicted by DFT, one can solve for a and b , which is shown in Table I. The high-pressure phase boundary of the S-III phase ($P_{\text{Expt}}^{\text{higher}}$) was determined to be 104 GPa in Fig. 5(f).

- [1] P. Monceau, Electronic crystals: An experimental overview, *Adv. Phys.* **61**, 325 (2012).
- [2] G. Grüner, The dynamics of charge-density waves, *Rev. Mod. Phys.* **60**, 1129 (1988).
- [3] S. Hellmann, T. Rohwer, M. Kalläne, K. Hanff, C. Sohr, A. Stange, A. Carr, M. M. Murnane, H. C. Kapteyn, L. Kipp, M. Bauer, and K. Rossnagel, Time-domain classification of charge-density-wave insulators, *Nat. Commun.* **3**, 1069 (2012).
- [4] H. G. Smith, N. Wakabayashi, W. P. Crummett, R. M. Nicklow, G. H. Lander, and E. S. Fisher, Observation of a charge-density-wave in α -U at low temperature, *Phys. Rev. Lett.* **44**, 1612 (1980).
- [5] Y. Akahama, M. Kobayashi, and H. Kawamura, Pressure-induced structural phase transition in sulfur at 83 GPa, *Phys. Rev. B* **48**, 6862 (1993).
- [6] H. Luo, R. G. Greene, and A. L. Ruoff, β -Po phase of sulfur at 162 GPa: X-ray diffraction study to 212 GPa, *Phys. Rev. Lett.* **71**, 2943 (1993).
- [7] O. Degtyareva, M. V. Magnitskaya, J. Kohanoff, G. Profeta, S. Scandolo, M. Hanfland, M. I. McMahon, and E. Gregoryanz, Competition of charge-density waves and superconductivity in sulfur, *Phys. Rev. Lett.* **99**, 155505 (2007).
- [8] O. Degtyareva, E. Gregoryanz, M. Somayazulu, H.-K. Mao, and R. J. Hemley, Crystal structure of the superconducting phases of S and Se, *Phys. Rev. B* **71**, 214104 (2005).
- [9] Y. Akahama, M. Kobayashi, and H. Kawamura, X-ray diffraction study on pressure-induced successive phase transition in selenium, *Solid State Commun.* **83**, 269 (1992).
- [10] M. I. McMahon, C. Hejny, J. S. Loveday, L. F. Lundegaard, and M. Hanfland, Confirmation of the incommensurate nature of Se-IV at pressures below 70 GPa, *Phys. Rev. B* **70**, 054101 (2004).
- [11] G. Parthasarathy and W. B. Holzapfel, High-pressure structural phase transitions in tellurium, *Phys. Rev. B* **37**, 8499 (1988).
- [12] C. Hejny and M. I. McMahon, Large structural modulations in incommensurate Te-III and Se-IV, *Phys. Rev. Lett.* **91**, 215502 (2003).
- [13] Y. Fujii, K. Hase, Y. Ohishi, H. Fujihisa, N. Hamaya, K. Takemura, O. Shimomura, T. Kikegawa, Y. Amemiya, and T. Matsushita, Evidence for molecular dissociation in bromine near 80 GPa, *Phys. Rev. Lett.* **63**, 536 (1989).
- [14] T. Kume, T. Hiraoka, Y. Ohya, S. Sasaki, and H. Shimizu, High pressure raman study of bromine and iodine: Soft phonon in the incommensurate phase, *Phys. Rev. Lett.* **94**, 065506 (2005).
- [15] K. Takemura, S. Minomura, O. Shimomura, and Y. Fujii, Observation of molecular dissociation of iodine at high pressure by x-ray diffraction, *Phys. Rev. Lett.* **45**, 1881 (1980).
- [16] T. Kenichi, S. Kyoko, F. Hiroshi, and O. Mitsuko, Modulated structure of solid iodine during its molecular dissociation under high pressure, *Nature (London)* **423**, 971 (2003).
- [17] K. Takemura, K. Sato, H. Fujihisa, and M. Onoda, Incommensurately modulated phase of iodine under high pressure, *Ferroelectrics* **305**, 103 (2004).
- [18] H. Fujihisa, K. Takemura, M. Onoda, and Y. Gotoh, Two intermediate incommensurate phases in the molecular dissociation process of solid iodine under high pressure, *Phys. Rev. Res.* **3**, 033174 (2021).
- [19] Y. Akahama, M. Kobayashi, and H. Kawamura, Simple-cubic-simple-hexagonal transition in phosphorus under pressure, *Phys. Rev. B* **59**, 8520 (1999).
- [20] H. Fujihisa, Y. Akahama, H. Kawamura, Y. Ohishi, Y. Gotoh, H. Yamawaki, M. Sakashita, S. Takeya, and K. Honda, Incommensurate structure of phosphorus phase IV, *Phys. Rev. Lett.* **98**, 175501 (2007).

- [21] R. J. Husband, I. Loa, K. A. Munro, E. E. McBride, S. R. Evans, H.-P. Liermann, and M. I. McMahon, Incommensurate-to-incommensurate phase transition in Eu metal at high pressures, *Phys. Rev. B* **90**, 214105 (2014).
- [22] X. Li, X. Huang, X. Wang, M. Liu, G. Wu, Y. Huang, X. He, F. Li, Q. Zhou, B. Liu, and T. Cui, High-pressure dissociation of selenium and tellurium, *Phys. Chem. Chem. Phys.* **20**, 6116 (2018).
- [23] M. D. Johannes and I. I. Mazin, Fermi surface nesting and the origin of charge density waves in metals, *Phys. Rev. B* **77**, 165135 (2008).
- [24] O. Degtyareva, E. Gregoryanz, H. K. Mao, and R. J. Hemley, Crystal structure of sulfur and selenium at pressures up to 160 GPa, *High Press. Res.* **25**, 17 (2005).
- [25] C. Hejny, L. F. Lundegaard, S. Falconi, M. I. McMahon, and M. Hanfland, Incommensurate sulfur above 100 GPa, *Phys. Rev. B* **71**, 020101(R) (2005).
- [26] O. Degtyareva, E. Gregoryanz, M. Somayazulu, P. Dera, H. Mao, and R. J. Hemley, Novel chain structures in group VI elements, *Nat. Mater.* **4**, 152 (2005).
- [27] M. Klein, Light scattering studies of incommensurate transitions, in *Light Scattering Near Phase Transitions*, Modern Problems in Condensed Matter Sciences, Vol. 5, edited by H. Cummins and A. Levanyuk (Elsevier, Amsterdam, 1983), Chap. 8, pp. 503–529.
- [28] H. Z. Cummins, Experimental studies of structurally incommensurate crystal phases, *Phys. Rep.* **185**, 211 (1990).
- [29] C. Marini, D. Chermisi, M. Lavagnini, D. Di Castro, C. Petrillo, L. Degiorgi, S. Scandolo, and P. Postorino, High-pressure phases of crystalline tellurium: A combined Raman and *ab initio* study, *Phys. Rev. B* **86**, 064103 (2012).
- [30] Y. Akahama and H. Kawamura, Pressure calibration of diamond anvil Raman gauge to 310 GPa, *J. Appl. Phys.* **100**, 043516 (2006).
- [31] S. J. Clark, M. D. Segall, C. J. Pickard, P. J. Hasnip, M. I. J. Probert, K. Refson, and M. C. Payne, First Principles Methods using CASTEP, *Z. Kristall.* **220**, 567 (2005).
- [32] P. Giannozzi, S. Baroni, N. Bonini, M. Calandra, R. Car, C. Cavazzoni, D. Ceresoli, G. L. Chiarotti, M. Cococcioni, I. Dabo, A. D. Corso, S. de Gironcoli, S. Fabris, G. Fratesi, R. Gebauer, U. Gerstmann, C. Gougoussis, A. Kokalj, M. Lazzeri, L. Martin-Samos *et al.*, QUANTUM ESPRESSO: A modular and open-source software project for quantum simulations of materials, *J. Phys.: Condens. Matter* **21**, 395502 (2009).
- [33] M. Monni, F. Bernardini, A. Sanna, G. Profeta, and S. Massidda, Origin of the critical temperature discontinuity in superconducting sulfur under high pressure, *Phys. Rev. B* **95**, 064516 (2017).
- [34] A. P. Drozdov, M. I. Erements, I. A. Troyan, V. Ksenofontov, and S. I. Shylin, Conventional superconductivity at 203 kelvin at high pressures in the sulfur hydride system, *Nature* **525**, 73 (2015).
- [35] J. Whaley-Baldwin and R. Needs, First-principles high pressure structure searching, longitudinal-transverse mode coupling and absence of simple cubic phase in sulfur, *New J. Phys.* **22**, 023020 (2020).
- [36] L. Zheng, Z. Wu, Y. Yang, L. Nie, M. Shan, K. Sun, D. Song, F. Yu, J. Li, D. Zhao, S. Li, B. Kang, Y. Zhou, K. Liu, Z. Xiang, J. Ying, Z. Wang, T. Wu, and X. Chen, Emergent charge order in pressurized kagome superconductor CsV₃Sb₅, *Nature (London)* **611**, 682 (2022).
- [37] M. Ido, Y. Okayama, T. Ijiri, and Y. Okajima, Pressure effect on the charge-density waves and the superconductivity in NbSe₃, *J. Phys. Soc. Jpn.* **59**, 1341 (1990).
- [38] C. Putzke, J. Ayres, J. Buhot, S. Licciardello, N. E. Hussey, S. Friedemann, and A. Carrington, Charge order and superconductivity in underdoped YBa₂Cu₃O_{7- δ} under pressure, *Phys. Rev. Lett.* **120**, 117002 (2018).
- [39] C. Proust and L. Taillefer, The remarkable underlying ground states of cuprate superconductors, *Annu. Rev. Condens. Matter Phys.* **10**, 409 (2019).
- [40] J. Chang, E. Blackburn, A. T. Holmes, N. B. Christensen, J. Larsen, J. Mesot, R. Liang, D. A. Bonn, W. N. Hardy, A. Watenphul, M. v. Zimmermann, E. M. Forgan, and S. M. Hayden, Direct observation of competition between superconductivity and charge density wave order in YBa₂Cu₃O_{6.67}, *Nat. Phys.* **8**, 871 (2012).
- [41] J. Wilson, F. D. Salvo, and S. Mahajan, Charge-density waves and superlattices in the metallic layered transition metal dichalcogenides, *Adv. Phys.* **24**, 117 (1975).
- [42] O. Moulding, I. Osmond, F. Flicker, T. Muramatsu, and S. Friedemann, Absence of superconducting dome at the charge-density-wave quantum phase transition in 2H-NbSe₂, *Phys. Rev. Res.* **2**, 043392 (2020).
- [43] R. Grasset, T. Cea, Y. Gallais, M. Cazayous, A. Sacuto, L. Cario, L. Benfatto, and M.-A. Méasson, Higgs-mode radiance and charge-density-wave order in 2H - NbSe₂, *Phys. Rev. B* **97**, 094502 (2018).
- [44] R. Grasset, Y. Gallais, A. Sacuto, M. Cazayous, S. Mañas-Valero, E. Coronado, and M.-A. Méasson, Pressure-induced collapse of the charge density wave and Higgs mode visibility in 2H-TaS₂, *Phys. Rev. Lett.* **122**, 127001 (2019).
- [45] R. J. Hemley, J. Shu, M. A. Carpenter, J. Hu, H. K. Mao, and K. J. Kingma, Strain/order parameter coupling in the ferroelastic transition in dense SiO₂, *Solid State Commun.* **114**, 527 (2000).
- [46] R. M. Fernandes, P. P. Orth, and J. Schmalian, Intertwined vestigial order in quantum materials: Nematicity and beyond, *Annu. Rev. Condens. Matter Phys.* **10**, 133 (2019).
- [47] S. Friedemann, W. J. Duncan, M. Hirschberger, T. W. Bauer, R. Kuchler, A. Neubauer, M. Brando, C. Pfleiderer, and F. M. Grosche, Quantum tricritical points in NbFe₂, *Nat. Phys.* **14**, 62 (2018).
- [48] C. Pépin, D. Chakraborty, M. Grandadam, and S. Sarkar, Fluctuations and the Higgs mechanism in underdoped cuprates, *Annu. Rev. Condens. Matter Phys.* **11**, 301 (2020).
- [49] S. Friedemann (2023): Dataset for publication Raman Spectroscopy Sulfur, available at the University of Bristol data repository, <https://doi.org/10.5523/bris.2ramvba12cngh2mujzqsjz2vik>.